ADVANCED SCIENCE Open Access
www.advancedscience.com

Dramatically Enhanced Valley-Polarized Emission by Alloying and Electrical Tuning of Monolayer $WTe_{2x}S_{2(1-x)}$ Alloys at Room Temperature with 1T′-WTe_2-Contact

Wei-Hsiang Lin, Chia-Shuo Li, Chih-I Wu, George R. Rossman, Harry A. Atwater,* and Nai-Chang Yeh**

Monolayer ternary tellurides based on alloying different transition metal dichalcogenides (TMDs) can result in new two-dimensional (2D) materials ranging from semiconductors to metals and superconductors with tunable optical and electrical properties. Semiconducting $WTe_{2x}S_{2(1-x)}$ monolayer possesses two inequivalent valleys in the Brillouin zone, each valley coupling selectively with circularly polarized light (CPL). The degree of valley polarization (DVP) under the excitation of CPL represents the purity of valley polarized photoluminescence (PL), a critical parameter for opto-valleytronic applications. Here, new strategies to efficiently tailor the valley-polarized PL from semiconducting monolayer $WTe_{2x}S_{2(1-x)}$ at room temperature (RT) through alloying and back-gating are presented. The DVP at RT is found to increase drastically from < 5% in WS_2 to 40% in $WTe_{0.12}S_{1.88}$ by Te-alloying to enhance the spin-orbit coupling. Further enhancement and control of the DVP from 40% up to 75% is demonstrated by electrostatically doping the monolayer $WTe_{0.12}S_{1.88}$ via metallic 1T′-WTe_2 electrodes, where the use of 1T′-WTe_2 substantially lowers the Schottky barrier height (SBH) and weakens the Fermi-level pinning of the electrical contacts. The demonstration of drastically enhanced DVP and electrical tunability in the valley-polarized emission from 1T′-WTe_2/$WTe_{0.12}S_{1.88}$ heterostructures paves new pathways towards harnessing valley excitons in ultrathin valleytronic devices for RT applications.

1. Introduction

Monolayer 1H-phase transition metal dichalcogenides (TMDs) such as WS_2 are direct band gap semiconductors that consist of an atomic layer of tungsten sandwiched between a top and a bottom layer of sulfur atoms that are arranged in their respective hexagonal lattice structure.[1,2] The band structures of monolayer TMDs[3–7] consist of two inequivalent K (−K) valleys in the hexagonal Brillouin zone. The strong spin-orbit coupling and broken inversion symmetry in monolayer TMDs result in a large energy splitting between the top spin-up (spin-down) valence band and the bottom spin-down (spin-up) valence band in the K (−K) valley via the preservation of time reversal symmetry.[8–13] Given that both of the Berry curvature and orbital magnetic moment are odd under the time-reversal symmetry operation, one can selectively populate excitons in different valleys (K or −K) by means of circularly polarized light (CPL), where CPL with positive helicity (σ^+) couples to the K valley and that of the negative helicity (σ^-) couples to the −K valley according to valley-dependent

W.-H. Lin, H. A. Atwater
Department of Applied Physics
California Institute of Technology
Pasadena, CA 91125, USA
E-mail: whlin@alumni.caltech.edu; haa@caltech.edu
C.-S. Li, C.-I Wu
Graduate Institute of Photonics and Optoelectronics and Department of Electrical Engineering
National Taiwan University
Taipei, Taiwan 106, P. R. China
The ORCID identification number(s) for the author(s) of this article can be found under https://doi.org/10.1002/advs.202304890
G. R. Rossman
Department of Geological and Planetary Sciences
California Institute of Technology
Pasadena, CA 91125, USA
N.-C. Yeh
Department of Physics
California Institute of Technology
Pasadena, CA 91125, USA
E-mail: ncyeh@caltech.edu
N.-C. Yeh
Kavli Nanoscience Institute
California Institute of Technology
Pasadena, CA 91125, USA

© 2023 The Authors. Advanced Science published by Wiley-VCH GmbH. This is an open access article under the terms of the Creative Commons Attribution License, which permits use, distribution and reproduction in any medium, provided the original work is properly cited.

DOI: 10.1002/advs.202304890

optical selection rules.[14–16] However, the degree of valley polarized emission in monolayer TMDs under CPL depends strongly on the intervalley scatterring time and exciton lifetimes. Therefore, understanding the processes that govern the exciton lifetimes and the associated degree of valley polarization is essential for assessing the emergent applications of valley-polarized excitons in devices.[17] Various strategies aiming at enhancing the valley polarization by further breaking the spatial-inversion symmetry have been proposed, including applying magnetic fields, chemical doping of magnetic elements, and employing magnetic proximity effects.[17–22] However, with respect to these methods for enhancing the valley polarization, the efficiency of applying an external magnetic field is extremely low for valley polarization (≈0.3 meV per Tesla); magnetic doping suffers from the formation of inhomogeneously distributed dopant clusters; and magnetic proximity effects are easily diminished by the valley submergence. Alternative approaches by electrical and optical control of the valley polarization in TMDs at room temperature and under off-resonance conditions would be more practical and desirable.[13,17] Towards this goal, carrier doping, including chemical and physical approaches, appears to be an efficient way to manipulate the valley polarization, because excess carriers introduced in the TMDs not only tailor the exciton species but also modify the valley polarization dynamics considerably. Chemical doping is known to be an effective and convenient method to modify the carrier concentrations and electronic bandstructures in monolayer TMD materials, which can induce shifts in the Fermi level as well as modifications to the electronic, optical, and valley polarization properties. Physcial doping, via either electrostatic carrier doping by gating or light excitation by creating electron-hole pairs, can also induce valley polarization enhancement through stronger screening of the Coulomb interaction by excess carriers, which helps suppress the intervalley scattering.[17]

For effective manipulation of the valley degrees of freedom in semiconducting monolayer TMDs by electrostatic doping, it is essential to address the interfacial issues of Fermi level pinning and Schottky barrier heights when making electrical contacts to the TMDs. To date, several approaches to circumvent these issues in TMD-based field effect transistors (FETs) have been reported, including the use of a low work function (WF) metal for the electrical contact,[23,24] the use of a Fermi-level de-pinning layer,[25,26] and various techniques of molecule/chemical doping of TMDs.[27–32] Developing heterostructures that consist of a two-dimensional (2D) van der Waals (vdW) metal as the top contact material on a 2D semiconductor is another approach to lower the Schottky barrier height (SBH).[33–36] For this purpose, a natural material for consideration is graphene.[37] However, deposition of another metallic layer on graphene is required for electrical characterizations, and the carrier injection efficiency generally varies, depending on the metal deposited. Alternatively, the metallic 1T′-phase WTe_2 with a low WF[38] and a vdW clean surface[39] may be considered as an efficient electron-type (*n*-type) contact material for 2D semiconductors. However, there have not been extensive studies to date on using the 1T′-phase WTe_2 as the metal contact to lower the contact resistance of TMD-based devices due to the challenges of material preparation and material stability.[40–43]

In this study, ternary $WTe_{2x}S_{2(1-x)}$ ($0 \le x \le 1$) alloys were synthesized via chemical vapor deposition in a one-step synthesis process to produce high-quality 2D semiconductors of tunable bandgaps for high-performance eletronic devices. By alloying Te into tungsten disulfide WS_2, the WF of the ternary $WTe_{2x}S_{2(1-x)}$ ($0 \le x \le 1$) alloy could be tuned to match that of the 2D contacts as the source (S) / drain (D) electrodes in the FET structure to reduce the SBH. These monolayer ternary $WTe_{2x}S_{2(1-x)}$ ($0 \le x \le 1$) alloys evolved from the semiconducting 1H phase to the metallic 1T′ phase, depending on the Te concentration (x). X-ray photoelectron spectroscopic (XPS) characterizations confirmed the existence of W, S, and Te with controlled ratios. The optical bandgap of the $WTe_{2x}S_{2(1-x)}$ alloy could be tuned from 2 to 1.65 eV in the 1H semiconducting phase and then dropped down to 0 in the 1T′ metallic phase. The FET devices based on monolayer $WTe_{2x}S_{2(1-x)}$ alloys revealed characteristics that confirmed the 1H phase being n-type semiconductors and the 1T′ phase being a metal. Moreover, the use of WTe_2 metallic contacts with a WF close to the band edge of the $WTe_{0.12}S_{1.88}$ alloy resulted in $WTe_{2x}S_{2(1-x)}$-based FETs with excellent electronic characteristics, including a high electron carrier mobility up to 50 $cm^2V^{-1}S^{-1}$ and an on/off current ratio up to 10^6. Furthermore, it has been reported that valley polarization can be tuned by doping,[44] defects,[13,45] and alloying engineering.[46] In particular, alloying with heavier elements can modify the valley polarization by enhancing the spin-orbit coupling (SOC). Therefore, it is worth investigating how the valley polarized emission from $WTe_{2x}S_{2(1-x)}$ alloys under CPL evolves with the concentration of Te. We note that the degree of valley polarization (DVP) for as-grown monolayer WS_2 is typically very low (<5%) at RT due to significant phonon- and defect-induced inter-valley scattering (**Figure 1**a), where the DVP value (P_{DVP}) is defined by the following expression:

$$P_{DVP} = \frac{I(\sigma^+) - I(\sigma^-)}{I(\sigma^+) + I(\sigma^-)} \quad (1)$$

with $I(\sigma^+)$ and $I(\sigma^-)$ denoting the right-handed (RH) and left-handed (LH) circular polarization-resolved photoluminescence (PL) intensity, respectively. In contrast, the P_{DVP} values in monolayer ternary alloys $WTe_{2x}S_{2(1-x)}$ with $x > 0$ were found to be tunable and were enhanced up to 40% under the excitation of right-handed circularly polarized (RCP) light. The underlying mechanism for tailoring the valley-polarized PL of monolayer 1H-ternary $WTe_{2x}S_{2(1-x)}$ alloys may be attributed to the enhanced SOC strength and broken mirror symmetry by mixing the Te-S species, as schematically shown in Figure 1b. The stronger SOC of the Te atoms than that of the S atoms can increase the spin-orbit energy splitting (Δ_{SO}) so that Δ_{SO} (WTe_2) = 484 meV and Δ_{SO} (WS_2) = 412 meV.[42] Additionally, by applying a back-gated voltage V_G to $WTe_{2x}S_{2(1-x)}$-based FETs with 1T′-WTe_2 as the contact electrodes, the resulting DVP values were found to be further enhanced from 40% for $V_G = 0$ up to ≈75% for $V_G = -20$ V. This finding suggests that modulating the carrier doping level can enhance the valley polarization by screening the long-range electron-hole exchange interactions, thus reducing the momentum-dependent intervalley scattering, as shown in Figure 1c. Overall, we have demonstrated successfully tuning and drastically enhancing the DVP values in semiconducting monolayer 1H-TMDs at RT by combined strategies of chemically alloying and electrically gating the monolayer TMD-based FETs with electrodes of reduced SBH and weakened

 © 2023 The Authors. Advanced Science published by Wiley-VCH GmbH

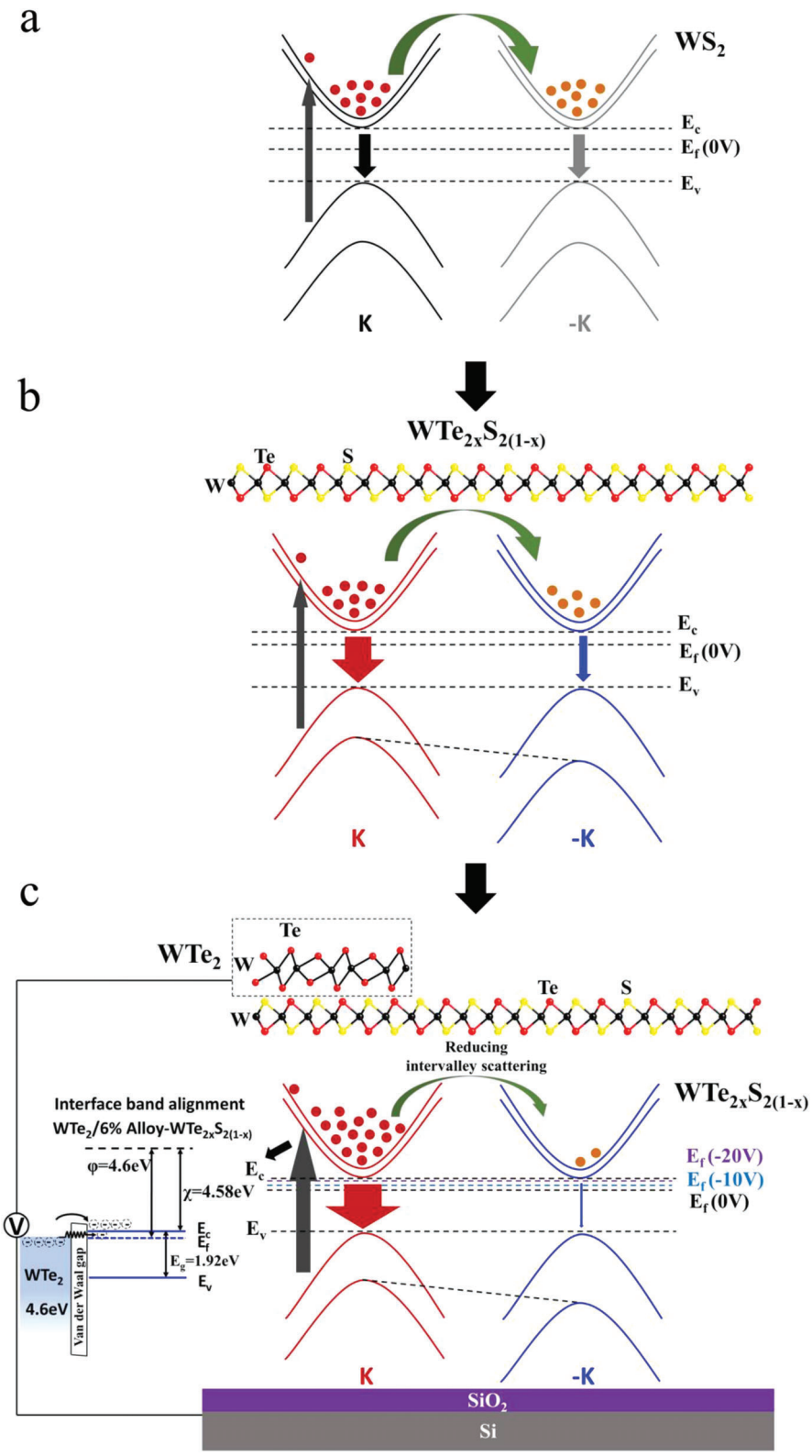

Figure 1. Proposed mechanism for tailoring the valley polarized PL of gated WTe_2/6%-$WTe_{2x}S_{2(1-x)}$ heterostructure: a) Schematics of the energy bands of monolayer WS_2 under right-handed CPL with significant intervalley scattering and therefore comparable decay rates for both σ^+ and σ^- excitons. b) Schematics of the energy bands of monolayer 6%-$WTe_{2x}S_{2(1-x)}$ under right-handed CPL, showing a significantly increased decay rate for σ^+ excitons. c) Schematics of the energy bands of a gated 6%-$WTe_{2x}S_{2(1-x)}$/WTe_2 heterostructure, showing both an increased decay rate of σ^+ excitons and suppressed intervalley scattering due to carrier doping-induced screening of the long-range electron-hole interaction.

 © 2023 The Authors. Advanced Science published by Wiley-VCH GmbH

Fermi level pinning. Our approach thus offers new opportunities toward developing realistic valley-dependent optoelectronic devices for energy-efficient information processing at room temperature.

2. Results and Discussion

The experimental setup for the growth of monolayer $WTe_{2x}S_{2(1-x)}$ ($0 \le x \le 1$) alloys is schematically depicted in Supporting Information Figure S1a (see details of the synthesis process in the Experimental Section). By tuning the ratios of the chalcogen precursors and that of the Ar/H_2 gas flow, we were able to synthesize both 1H and 1T′ phases of monolayer $WTe_{2x}S_{2(1-x)}$ ($0 \le x \le 1$). **Figure 2**a–d show typical optical microscopy (OM) images of the 1H and 1T′ $WTe_{2x}S_{2(1-x)}$ monolayers. When the chalcogen ratio (Te/S) increased from 1 to 7 and the Ar/H_2 ratio increased from 80/40 to 80/50, monolayer 1T′ $WTe_{2x}S_{2(1-x)}$ was obtained. The reactivity of the Te with WO_3 was far lower than that of S with WO_3, so the usage of a large amount of Te precursors and higher H_2 gas flow was necessary to ensure that Te could be incorporated into the $WTe_{2x}S_{2(1-x)}$ matrix to form the 1T′ phase.

X-ray photoelectron spectroscopic (XPS) was used to investigate the chemical composition of the $WTe_{2x}S_{2(1-x)}$ ($0 \le x \le 1$) alloys synthesized by atmosphere-pressure chemical vapor deposition (APCVD) and to evaluate the electron doping concentration as a function of the Te doping concentration. The core level spectra were calibrated via fitting adventitious carbon at 284.8 eV. The high-resolution spectra of W 4f, S 2p, and Te 3d peaks are shown in Figure 2e–g. For 1H-phase WS_2, the corresponding binding energies of the W $4f_{7/2}$ and W $4f_{5/2}$ peaks were located at 33.2 and 35.3 eV, respectively, and the binding energies for the S $2p_{3/2}$ and S $2p_{1/2}$ peaks were located at 162.9 and 164.2 eV, respectively, which were all consistent with the values reported previously.[47] By tuning the mass ratios of Te and S powder from 1 to 100 with specific H_2 flow rates from 40 to 60 sccm during the synthesis process, W-Te bonds at 573.8 eV (Te $3d_{5/2}$) and 584.1 eV (Te $3d_{3/2}$) appeared in the spectra, which provided direct evidence for Te doping into the original WS_2 crystal lattice. The binding energy of W 4f and S 2p peaks displayed a downshift ≈0.4 eV in the alloy with $x = 13\%$, indicating that Te doping resulted in reduced electronegativity. When a structural phase transition occurred at a higher stoichiometric ratio ($x > 0.5$), the binding energies of W 4f, S 2p, and Te 3d all shifted to lower energy states concurrently. For 1T′-phase WTe_2, the main W 4f peaks at 31.28 eV ($4f_{7/2}$) and 33.44 eV($4f_{5/2}$) and the Te 3d peaks located at 572.6 ($3d_{5/2}$) and 583 eV ($3d_{3/2}$) were assigned to the W–Te bond. The chemical stoichiometry information mentioned above directly indicated that the mole fraction of Te and the structural evolution between the 1H and 1T′ phases could be tuned by changing the mass ratio of Te and S powder together with specific H_2 concentrations during the APCVD growth. Furthermore, the distinct binding energy redshifts of W 4f, Te 3d, and S 2p with increasing Te concentration up to $x = 35\%$ indicate that the Fermi level moved downward closer to the valence band and hence the p-type doping of Te into the WS_2 lattice, which was further corroborated by measurements of the increasing work function of $WTe_{2x}S_{2(1-x)}$ with x for $0 < x \le 0.35$ by ultraviolet photoelectron spectroscopy (UPS, to be further elaborated below), as shown in the inset of **Figure 3**c. Both of the XPS and UPS showed that Te as the p-type dopant doped in the n-type semiconductor.

To quantitatively evaluate the changes in the electron carrier concentration with Te doping, which plays a critical role in determining the DVP of 1H-ternary $WTe_{2x}S_{2(1-x)}$ alloys ($0 < x \le 0.35$), we need to evaluate the $(E_c - E_F)$ values of $WTe_{2x}S_{2(1-x)}$, where E_c and E_F denote the conduction band edge energy and the Fermi level, respectively. We employed the UPS studies to extract the $(E_F - E_v)$ values and the PL measurements to obtain the optical bandgap $E_{emission}$ values for $WTe_{2x}S_{2(1-x)}$ ($0 < x \le 0.35$), where E_v denotes the valance band edge energy, and the bandgap between the conduction and valence band edges is given by $E_g \equiv (E_c - E_v) = E_{emission} + E_{binding}$, where $E_{binding}$ represents the binding energy of A-excitons. As shown in Figure 2h, linear extraction of the valence band edge tail was used to determine the $(E_F - E_v)$ values. We found that the $(E_F - E_v)$ value first increased from 1.8 eV for $x = 0$ to 1.9 eV for $x = 6\%$, and then steadily decreased with increasing x down to 1.57 eV for $x = 35\%$, as shown in Figure 2h,i.

Next, using the optical bandgap $E_{emission}$ of the 1H-$WTe_{2x}S_{2(1-x)}$ obtained from the PL measurements (Figure 3b), and noting that $E_{emission} = (E_c - E_v) - E_{binding} = (E_c - E_F) + (E_F - E_v) - E_{binding}$ where $(E_F - E_v)$ were given by the UPS studies as mentioned above, we derived the $(E_c - E_F)$ values for the 1H-$WTe_{2x}S_{2(1-x)}$ by using $E_{binding} = Ry\,(\mu/m_e)\,(\epsilon_0/\epsilon_s)^2 \sim 0.1$ eV, with Ry being the Rydberg energy 13.6 eV, $\mu \sim 0.178\, m_e$ the reduced mass of A-excitons, m_e the free electron mass, and $(\epsilon_s/\epsilon_0) \sim 5$ the dielectric constant of the substrate. After the $(E_c - E_F)$ values were determined as a function of the Te doping, the electron doping concerntrations (N_D) may be calculated by using the effective density of state (N_C) near the bottom of the conduction band for two-dimensional electrons

$$N_C = \left(4\pi m_e^*/h^2\right) \tag{2}$$

where h is the Planck constant. Thus, we obtained N_D from the following expression

$$N_D = N_C k_B T \ln\left[1 + \exp\left(-\frac{E_c - E_F}{k_B T}\right)\right] \tag{3}$$

where T is the temperature and k_B is the Boltzmann constant. The results of the N_D analysis are presented in Figure 2j, showing that N_D decreases from (3×10^{10}) cm^{-2} to (1×10^7) cm^{-2} when varies the Te concentration from 6% to 35%, and that the Fermi level for all samples with $x \le 35\%$ was below E_c at room temperature. This analysis suggests that the carrier densities in the semiconducting 1H-$WTe_{2x}S_{2(1-x)}$ alloys may be controlled by tuning the Te doping level.

The optical properties of the $WTe_{2x}S_{2(1-x)}$ alloys were investigated by Raman and PL spectra, and the $E_{emission}$ values derived from the PL spectra were applied to estimating the $(E_c - E_F)$ values and the electron doping concentrations using Equations (2) and (3) as stated above. In Figure 3a, Raman spectra of the $WTe_{2x}S_{2(1-x)}$ alloys with various Te concentrations were collected to examine the composition-dependent lattice vibrational modes. For monolayer 1H-phase WS_2, the two characteristic peaks E^1_{2g} and A_{1g} were located at 351 cm^{-1} and 419 cm^{-1}, respectively, in agreement with previous reports.[13] In the 1H-phase alloys, it was evident that the Raman footprints

 © 2023 The Authors. Advanced Science published by Wiley-VCH GmbH

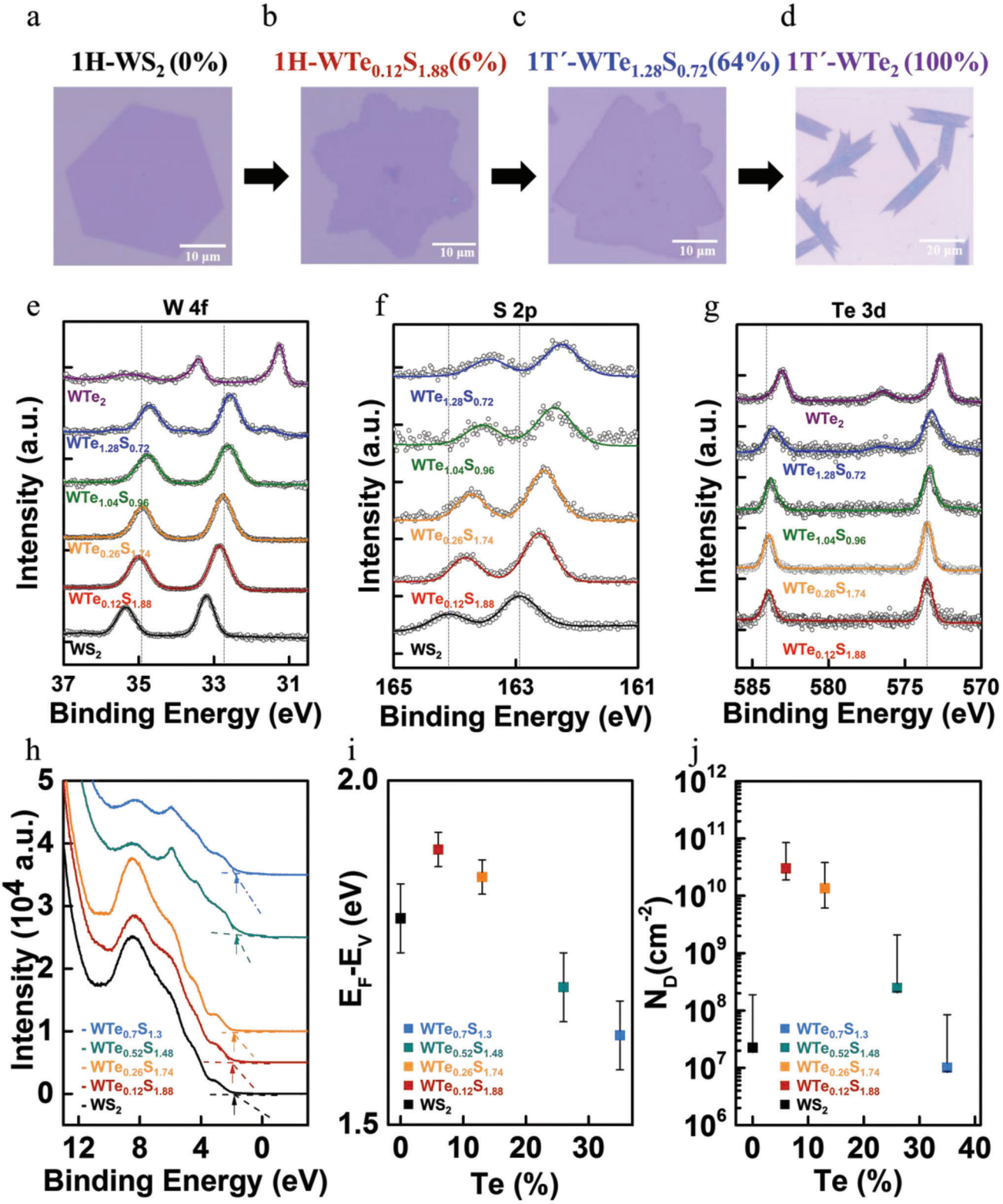

Figure 2. Optical microscopic images, chemical compositions and carrier doping of monolayer $WTe_{2x}S_{2(1-x)}$ alloys for a) 1H-WS_2, b) 1H-$WTe_{0.12}S_{1.88}$, c) 1T′- $WTe_{1.28}S_{0.72}$, d) 1T′- WTe_2. XPS spectra of monolayer $WTe_{2x}S_{2(1-x)}$ alloys with $x = 0$, 0.06, 0.13, 0.52, 0.64, and 1, respectively: e) XPS W 4f spectra, f) XPS S 2p spectra, and g) XPS Te 3d spectra. h) Valence band spectra with increasing Te doping concentration in $WTe_{2x}S_{2(1-x)}$ alloys. i) ($E_F - E_V$) values extracted from the UPS spectra in h) for $WTe_{2x}S_{2(1-x)}$ alloys with different x-values. j) Electron doping concentration versus Te doping concentration in $WTe_{2x}S_{2(1-x)}$ alloys by using the ($E_C - E_F$) values extracted from ultraviolet photoelectron spectroscopy (UPS) and PL spectra as explained in the main text.

 © 2023 The Authors. Advanced Science published by Wiley-VCH GmbH

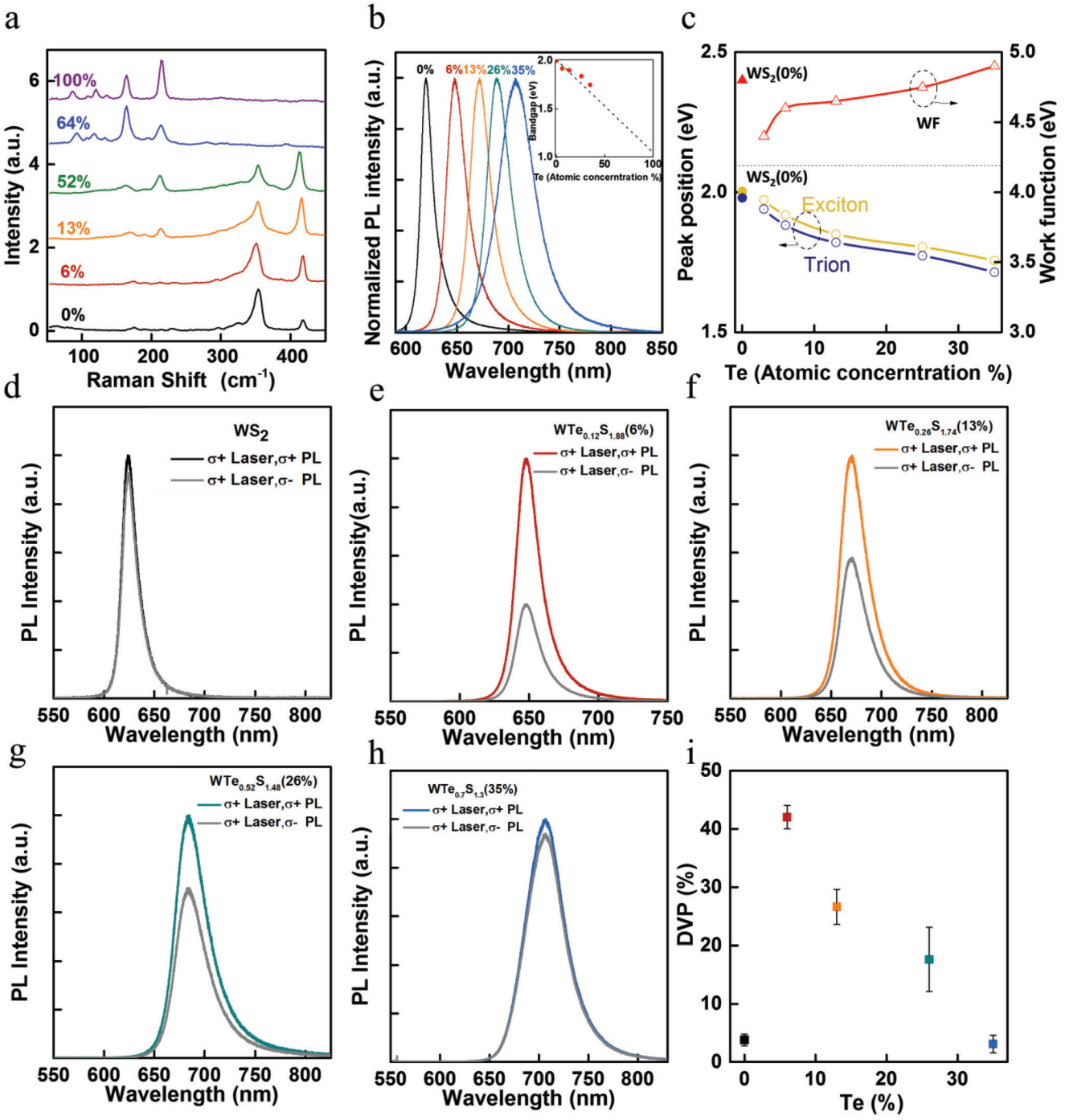

Figure 3. Raman, PL and valley-polarized PL spectra of monolayer $WTe_{2x}S_{2(1-x)}$ alloys: a) Raman spectra of the alloys with $x = 0$, 0.06, 0.13, 0.52, 0.64 and 1. b) PL spectra of monolayer $WTe_{2x}S_{2(1-x)}$ alloys with $x = 0$, 0.03, 0.06, 0.13, 0.26, and 0.35, respectively. The inset shows the corresponding composition-dependent (x) bandgap of the $WTe_{2x}S_{2(1-x)}$ alloys, as determined by PL. c) The peak positions of A-excitons and trions, and the corresponding work function of monolayer $WTe_{2x}S_{2(1-x)}$ alloys with $x = 0$, 0.06, 0.13, 0.26, and 0.35, respectively. Circularly polarized PL spectra of monolayer $WTe_{2x}S_{2(1-x)}$ alloys under the excitation of σ^+ light (514 nm) at RT: d) WS_2, e) $WTe_{0.12}S_{1.88}$, f) $WTe_{0.26}S_{1.74}$, g) $WTe_{0.52}S_{1.48}$, and h) $WTe_{0.7}S_{1.3}$. (i) DVP versus increasing Te doping concentration on $WTe_{2x}S_{2(1-x)}$ alloys extracted from (d) to (h), showing much enhanced DVP in $WTe_{0.12}S_{1.88}$, $WTe_{0.26}S_{1.74}$ and $WTe_{0.52}S_{1.48}$ relative to that in WS_2.

 © 2023 The Authors. Advanced Science published by Wiley-VCH GmbH

changed with increasing Te concentration relative to those of the pure WS_2, where the 1H-phase characteristic peaks weakened and additional peaks associated with the 1T′-phase appeared around 163 cm^{-1} and 213 cm^{-1}. The positions of the two WS_2 vibrational modes were softened and redshifted with the increase of Te concentration, which may be attributed to the effect of heavier Te atoms on decreasing the vibrational frequencies. In comparison with pure 1T′-WTe_2 with main A_1 modes[48] at 120, 132, 162, and 213 cm^{-1}, the observed new peaks around 195, 225, 290, and 400 cm^{-1} in Figure 3a were similar to the 1H-phase and 1T′-phase WS_2-like peaks reported previously.[49–53]

In addition to the Raman spectra, PL measurements were performed on the alloys to investigate the composition-dependent optical bandgap ($E_{emission}$) evolution and phase transition in Figure 3b. We found that the optical bandgap of the $WTe_{2x}S_{2(1-x)}$ alloys could be tuned from 2 eV (for pure 1H-WS_2) to zero (for pure 1T′-WTe_2) as the concentration of Te increased, and 1H to 1T′ phase transition existed at an intermediate Te concentration ($x > 0.35$) in the $WTe_{2x}S_{2(1-x)}$ alloys. For 1T′ ternary tellurides, no PL signal could be detected because of their metallic nature. Notably, within the 1H phase, the correlation between the optical bandgap and the Te concentration was approximately linear to each other, and the 1H-phase optical bandgap ranged between 2 eV (pure WS_2, $x = 0$) and 1.75 eV ($WTe_{2x}S_{2(1-x)}$ alloy, $x = 0.35$), as presented in the inset of Figure 3b. Additionally, the composition-dependent PL peak position of the as-grown alloys was found to be in good agreement with the quadratic rule of the bandgap (E_g) estimation reported by Kang et al:[54]

$$E_g(WTe_{2x}S_{2(1-x)}) = xE_g(WTe_2) + (1-x)E_g(WS_2) - bx(1-x) \quad (4)$$

where the parameter b for $WTe_{2x}S_{2(1-x)}$ alloy equals 0.08,[54] and the bandgap of the 1H-phase WTe_2 is 1.03 eV from literature.[7,55,56]

The validation of the correlation between the $E_{emission}$ value and the Te doping level in Equation (4) thus provides a fast and efficient way to determine the chemical composition of the $WTe_{2x}S_{2(1-x)}$ alloy. The neutral A-exciton PL peak of different $WTe_{2x}S_{2(1-x)}$ alloys, which resulted from direct-gap A-exciton recombination at the K/K′ points in the Brillouin zone, exhibited an approximately 250 meV redshift when doped with ≈ 35% Te. We also fitted the PL spectra of pure WS_2 and the 1H-phase $WTe_{2x}S_{2(1-x)}$ alloys ($x < 0.5$) to deconvolve (Supporting Information, Figure S2) the A-exciton and trion contributions, and found that the optimal lineshape for the spectral contributions was a mixed Gaussian–Lorentzian function. As shown in Figure 3c, the A-exciton and trion peaks of $WTe_{2x}S_{2(1-x)}$ alloys ($x < 0.5$) were both redshifted relative to those of pure WS_2, which was consistent with the decreasing optical bandgap with increasing Te doping.

Figure 3d–i show the polarization-dependent PL spectra of 1H phase monolayer WS_2 and $WTe_{2x}S_{2(1-x)}$ alloys on SiO_2/Si substrate under σ^+ circularly polarized excitation. The valley polarization of WS_2 at room temperature (RT) rarely exceeded 5%, but the DVP in monolayer ternary $WTe_{2x}S_{2(1-x)}$ ($x < 0.5$) alloys were found to vary from 3% (for x = 35%) to 40% (for x = 6%). The significant enhancement in the valley-polarization at RT from WS_2 to $WTe_{0.12}S_{1.88}$ may be attributed to the enhanced spin-orbit coupling by introducing Te atoms in WS_2 lattice. On the other hand, the substitutions of S atoms by Te atoms also markedly affect the carrier density. The estimated 2D carrier density versus Te-concentration is shown in Figure 2j, showing an initial rapid increase from $x = 0$ to $x = 6\%$ followed by a monotonic decreasing trend with a further increase in the Te-concentration. The Te-doping dependence of the 2D carrier density is similar to that of the DVP shown in Figure 3i, where the highest enhancement in the valley polarization (≈ 40%) at RT was found when the carrier density reached the highest value (≈3 × 10^{10}) cm^{-2} in the $WTe_{0.12}S_{1.88}$ ($x = 6\%$) alloy. Similar behavior of the DVP dependence on Te doping for $WTe_{2x}S_{2(1-x)}$ alloys is also found under σ^- circularly polarized excitation, as shown in Figure S3 (Supporting Information). This correlation between the carrier density and the DVP may be understood in terms of increasing exciton screening effects with increasing carrier densities, which resulted in reduced long-range electron-hole exchanging interactions and hence suppressed the momentum-dependent intervalley scattering and improved the DVP.

Noting the benefits of carrier doping and increased spin-orbit coupling on enhancing the DVP in $WTe_{0.12}S_{1.88}$, we conjectured that further enhancement of the DVP may be achieved by controlling the carrier densities via electrostatic doping, which would require the development of high-quality electrical contacts with reduced SBH and weakened Fermi level pinning to the 1H-$WTe_{2x}S_{2(1-x)}$ alloys. To this end, we fabricated back-gated FETs based on $WTe_{2x}S_{2(1-x)}$ alloys on (P++)Si/SiO_2 substrates and used specially designed electrical contacts to evaluate the performance of these devices, which provided critical information about the quality of our electrical contacts on the $WTe_{2x}S_{2(1-x)}$ alloys.

To fabricate 1H-$WTe_{2x}S_{2(1-x)}$ based FETs, monolayer $WTe_{2x}S_{2(1-x)}$ flakes were first transferred to heavily p-doped Si substrates with a SiO_2 top layer of 285 nm thickness, which served as a bottom gate and a gate dielectric, respectively. The metallic contact electrodes were fabricated by E-beam lithography, and 200 nm Au contact electrodes were deposited on silanol functionalized SiO_2/Si substrate using E-beam evaporation. The channel length (L) and width (W) of the fabricated devices were 0.5 μm and 1 μm (**Figure 4**a), respectively. The metallic contact electrodes were transferred and aligned on top of the $WTe_{2x}S_{2(1-x)}$ monolayer flake by means of a metal transferred method, to be elaborated in the experimental section. Using cross-sectional analysis by transmission electron microscopy (TEM), we examined the interface between the transferred Au and the monolayer $WTe_{2x}S_{2(1-x)}$ as shown in Figure 4b, and found that in contrast to the direct Au deposition onto monolayer TMD via electron-beam evaporation, our process of transferring Au contacts to $WTe_{2x}S_{2(1-x)}$ did not incur any damages to the $WTe_{2x}S_{2(1-x)}$ layer, as evidenced by the perfect rows of atoms clearly visible in the TEM image (Figure 4b). The electrical performance of the CVD-grown $WTe_{2x}S_{2(1-x)}$ alloys with metal-transferred Au contact electrodes was investigated by studying the backgated FETs made of monolayer $WTe_{2x}S_{2(1-x)}$ alloys. The transfer characteristic curves of the monolayer $WTe_{2x}S_{2(1-x)}$ devices are presented in Figure 4 and Figure S4, Supporting Information. In Figure 4c–e, all semiconducting 1H-phase $WTe_{2x}S_{2(1-x)}$ alloys (x = 0, 0.06, 0.13, 0.26, and 0.35) devices showed typical n-type transport behavior with high on/off (> 10^5) current ratios. Additionally,

 © 2023 The Authors. Advanced Science published by Wiley-VCH GmbH

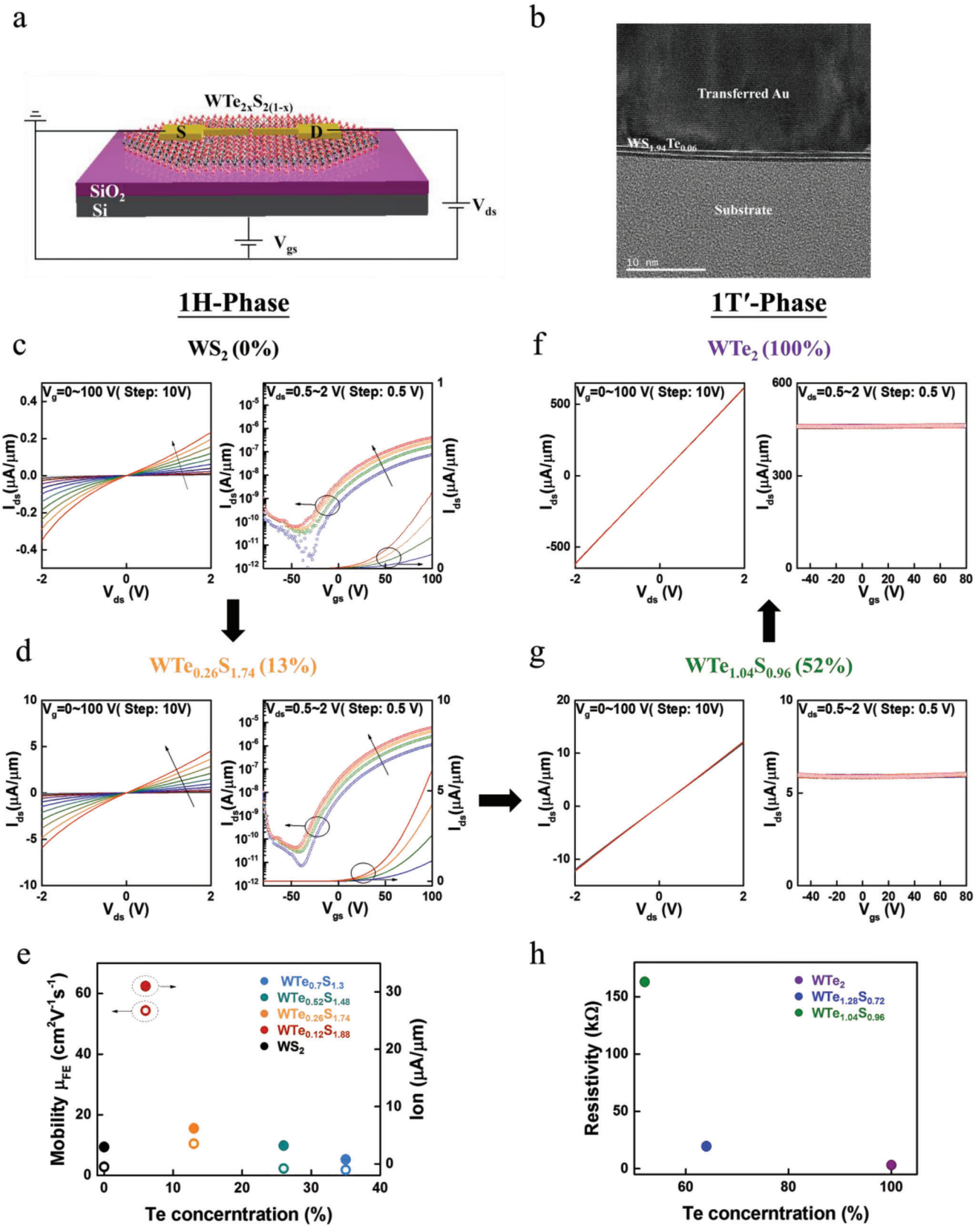

© 2023 The Authors. Advanced Science published by Wiley-VCH GmbH

the field-effect mobility (μ_{FE}) may be evaluated by the following relation:[57,58]

$$\mu_{FE} = \frac{L}{WV_{ds}C_g}\frac{dI_{ds}}{dV_{gs}} \quad (5)$$

where I_{ds} is the source-drain current, V_{gs} the gate-source voltage; V_{ds} the source-drain voltage, and C_g the gate capacitance. Using Equation (5) and the transfer characteristic curves in Figure 4c–e, we obtained mobility values of 0.58 $cm^2\ V^{-1}\ s^{-1}$, 35 $cm^2\ V^{-1}\ s^{-1}$, 10.5 $cm^2\ V^{-1}\ s^{-1}$, 2.8 $cm^2\ V^{-1}\ s^{-1}$, and 1.8 $cm^2\ V^{-1}\ s^{-1}$ for the 1H-phase $WTe_{2x}S_{2(1-x)}$ alloys with $x = 0$, 0.06, 0.13, 0.26, and 0.35, respectively. The ON current (I_{on}) for the $WTe_{0.12}S_{1.88}$ alloy-based devices was improved by 2 orders of magnitude relative to the control devices (WS_2-FET devices). In contrast, for the 1T′-phase alloys, the drain current was found to increase by ≈50 times in magnitude from the 1T′-phase $WTe_{2x}S_{2(1-x)}$ alloys ($x = 0.52$) to pure WTe_2, which implied that the metallic behavior of tellurides could be modified by controlling the concentration of the alloying S atoms. Furthermore, the source-drain current (I_{ds}) was completely independent of the backgated voltage (V_{gs}) in all three semimetallic 1T′-phase $WTe_{2x}S_{2(1-x)}$ alloys ($x = 0.52$, 0.64 and 1), as shown in Figure 4f–h, and the resistivity of the WTe_2 devices was reduced by 2 orders of magnitude as compared to that of the 1T′-phase $WTe_{2x}S_{2(1-x)}$ ($x = 0.52$) devices.

The improvement in the electrical performance of the FETs based on the 1H-phase semiconducting $WTe_{2x}S_{2(1-x)}$ alloys with Au electrode can be attributed to several effects. At the metal-semiconductor interface, electrons can be injected from the metal to the semiconductor either by thermionic emission over the Schottky barrier or via tunneling through the Schottky barrier. The width of the Schottky barrier is equal to the width of the depletion region (W_{dep}), which depends on the doping concentration (N_D) of the semiconductor and is proportional to $(N_D)^{-1/2}$according to the following relation: $W_{dep} = \sqrt{2\varepsilon_s V_{bi} d_{TMD}/(eN_D)}$, where $d_{TMD} \sim 0.6$ nm is the monolayer thickness of the TMD sample, ϵ_s (≈5) is the dielectric constant of semiconductors, $V_{bi} = (\phi_M - \phi_s)/e$ is the built-in potential between the metallic contact and the TMD semiconductor, and e is the elementary charge. Therefore, W_{dep} decreased with increasing N_D, and the probability of electron injection into the semiconductor via tunneling through the Schottky barrier increased. Indeed, we found the largest I_{on} and highest μ_{FE} in the lightly Te-doped FET devices ($WTe_{2x}S_{2(1-x)}$ with $x = 6\%$) because of the maximum N_D value $\sim(3 \times 10^{10})\ cm^{-2}$ that induced the minimum depletion width W_{dep}, which enhanced the electron tunneling through the Schottky barrier. Additionally, we note that the quality of the electrical contact between the metallic electrode and the semiconducting channel directly affects the carrier injection and therefore the performance of the devices. In the case of TMD-based devices, at the metal electrode/TMD interface, the large bandgap of TMDs leads to a Schottky barrier (SB) and a van der Waal (vdW) gap without chemical bonds, which gives rise to a high contact resistance for the as-fabricated devices. Thus, it is imperative to eliminate the interfacial vdW gap and to depin the Fermi level of the metallic electrode to facilitate efficient charge transport across the contact interface for optimized FET device performances as well as efficient control of electrostatic doping.

To overcome the Fermi level pinning effect and to lower the Schottky barrier height (SBH) at the interface, we developed a new process to transfer surface-functionalized, water-assisted wafer Au electrodes onto monolayer $WTe_{2x}S_{2(1-x)}$ to form $WTe_{2x}S_{2(1-x)}$-based FETs with Au contacts, as schematically illustrated in Figure S5. Besides using the Au contacts, there are two known methods to date for eliminating the Fermi-level pinning effects of electrical contacts to TMDs. One is to strengthen the hybridization by doping the underlying TMDs. The other is to weaken the hybridization between the contact electrode and the TMDs by inserting graphene to greatly reduce the contact resistance and SBH. The use of heterostructures that consist of a 2D van der Waals (vdW) semi-metal, such as graphene, as the top contact material on a 2D semiconductor, is a common approach to lower the SBH and contact resistance. However, deposition of another metallic layer on graphene is required for electrical characterizations, and the carrier injection efficiency generally varies, depending on the metal deposited on graphene. Alternatively, the metallic 1T′-phase WTe_2 with a low work function and a vdW clean surface may be an efficient electron-type (*n*-type) contact material for 2D semiconductors. However, there have not been extensive studies to date on using the 1T′-phase WTe_2 as the metal contact to lower the contact resistance of TMD-based devices because of the challenges in materials preparation and stability. Noting that Te-based monolayers are known to be unstable in ambient conditions, we chose multilayer WTe_2 as the electrodes alternative to Au contacts for the $WTe_{2x}S_{2(1-x)}$ alloy-based FET devices. The stability test of multilayer WTe_2 is illustrated in Figure S6 (Supporting Information), which demonstrates that multilayer WTe_2 could be stable in air beyond 15 days.

Next, we investigated the characteristics of the 1H-$WTe_{2x}S_{2(1-x)}$-based FETs with two types of transferred source(S)/drain(D) electrodes: Au (work function ≈ 5.2 eV), and 1T′-WTe_2 (work function ≈ 4.6 eV), as shown in **Figure 5**. Given that 1T′-WTe_2 has the closest electron affinity to the work function of 1H-$WTe_{0.12}S_{1.88}$, we expected the use of 1T′-WTe_2 electrodes to induce the lowest Schottky barrier height. The work function of each electrode was measured by ultraviolet photoelectron spectroscopy (UPS) and the results are shown in Figure S7, Supporting Information. Figure 5a,b illustrate the band diagrams of the Au/1H-$WTe_{0.12}S_{1.88}$ and 1T′-WTe_2/1H-$WTe_{0.12}S_{1.88}$ interfaces in the equilibrium condition after both of the contacts were made. The charge injection in the 2D $WTe_{0.12}S_{1.88}$ channel was determined by the SBH and Schottky barrier width (SBW), both largely

Figure 4. Transport characterizations of back-gated FET devices based on 1H-phase and 1T′-phase $WTe_{2x}S_{2(1-x)}$ alloys: a) Schematic illustration of a fabricated FET device. b) Cross-sectional image of the metal-semiconductor interface captured by transmission electron microscopy (TEM). Current-voltage (I_{ds} vs. V_{ds}) characteristics with different bottom gate voltage (V_g) and gating response (I_{ds} vs. V_{gs}) with different source-drain voltages (V_{ds}) from 0.5 V to 2 V for c) 1H-WS_2, and d) 1H-$WTe_{0.26}S_{1.74}$. e) Room-temperature μ_{FE} and I_{on} of monolayer semiconducting $WTe_{2x}S_{2(1-x)}$ alloys with x = 0, 0.06, 0.13, 0.26, and 0.35. Current-voltage (I_{ds} vs. V_{ds}) characteristics with different bottom gate voltage (V_g) and gating response (I_{ds} vs. V_{gs}) with different source-drain voltages (V_{ds}) from 0.5 V to 2 V for f) 1T′-$WTe_{1.04}S_{0.96}$ and g) 1T′-WTe_2. h) Room-temperature resistivity of monolayer metallic $WTe_{2x}S_{2(1-x)}$ alloys with $x = 0.52$, 0.64, and 1.

 © 2023 The Authors. Advanced Science published by Wiley-VCH GmbH

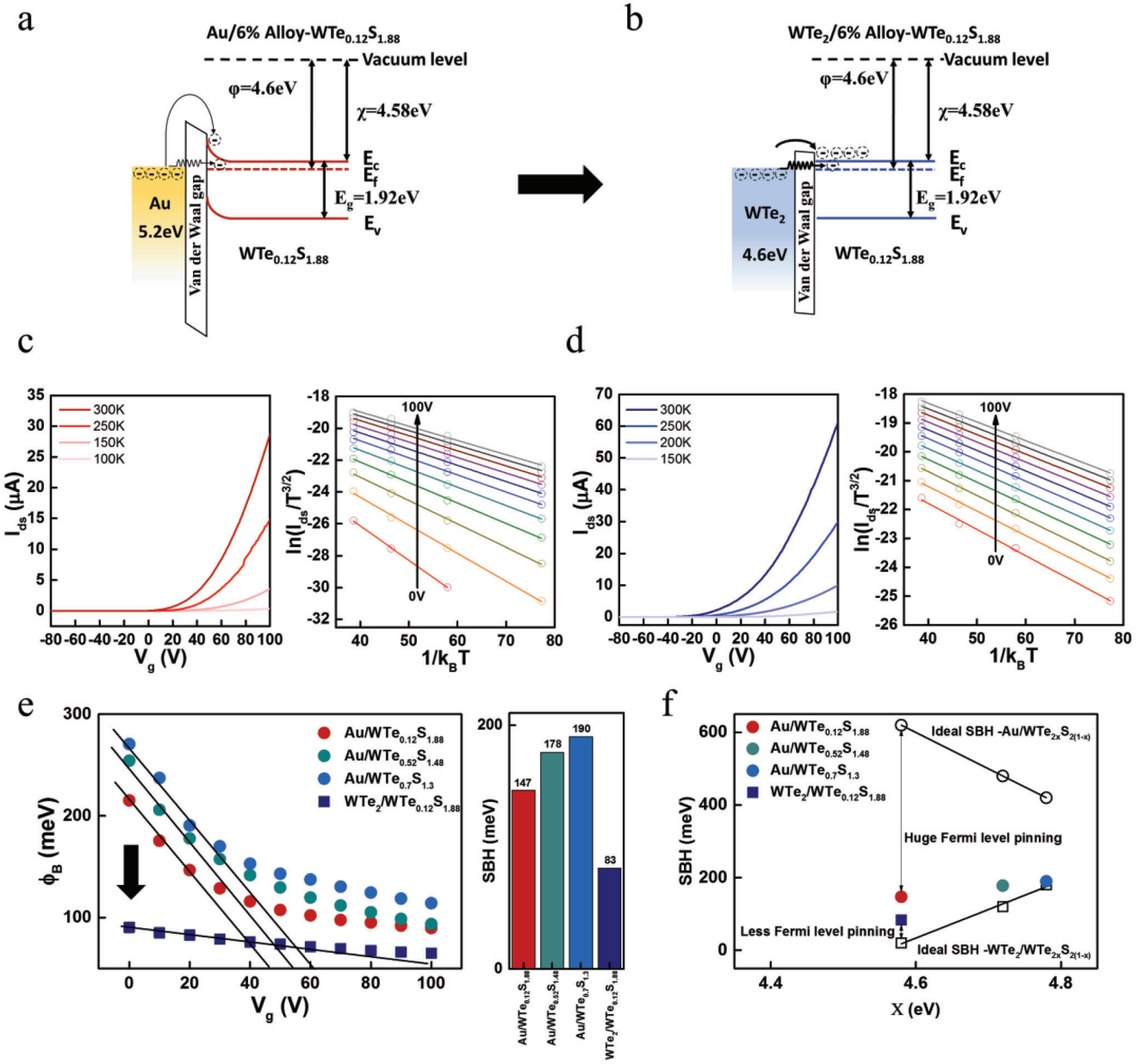

Figure 5. Schottky barrier height between metal electrodes (Au, WTe_2) and $WTe_{2x}S_{2(1-x)}$ alloys: a) Schematic band diagram of $WTe_{2x}S_{2(1-x)}$ FET interface with Au electrode obtained from UPS measurements. b) Schematic band diagram of $WTe_{2x}S_{2(1-x)}$ FET interface with 1T′-WTe_2 electrode obtained from UPS measurements. Temperature-dependent two-terminal current I_{ds} as a function of V_{gs} at V_{ds} = 2 V for the FET devices with c-left) Au, and d-left) WTe_2 electrical contacts. Gate-voltage-dependent ln ($I_0/T^{3/2}$) versus ($1/kT$) plot with two different contacts: c-right) Au, and d-right) WTe_2. From the slopes of the curves shown in Figure c), d) and Figure S7, the gate-voltage-dependent SBH (ϕ_B) of the FETs are extracted in e). f) Comparisons of the extracted SBH at V_{FB} of the monolayer 6%-$WTe_{2x}S_{2(1-x)}$ alloys with WTe_2 electrode and the monolayer $WTe_{2x}S_{2(1-x)}$ alloys with x = 0.06, 0.26, and 0.35 and Au electrode.

dependent on the extent of the semiconductor band-bending at the metal (Au or 1T′ WTe_2) and 1H-$WTe_{0.12}S_{1.88}$ Schottky contact region. While the SBH governed the extent of thermionic emission of carriers over the barrier, the SBW determined the extent of the thermionic field emission and quantum tunneling of charge carriers. Hence, both the SBH and SBW must be minimized to achieve efficient injection of charge carriers from the contact into the semiconducting $WTe_{0.12}S_{1.88}$ channel as shown in Figure 5b.

The field-effect mobility and the on/off current ratios of 1H-phase $WTe_{0.12}S_{1.88}$ crystal for Au and WTe_2 electrodes were found to be μ_{FE} = 35 $cm^2\ V^{-1}\ s^{-1}$ and (I_{on}/I_{off}) = 5×10^5, and μ_{FE} = 50 $cm^2\ V^{-1}\ s^{-1}$ and (I_{on}/I_{off}) = 1.1×10^6, respectively. In particular, we found substantially more efficient gate tunability in the FET with 1T′-WTe_2 contacts. That is a smaller threshold voltage $V_{g,th}$ of 18 V (compared with $V_{g,th}$ = 50 V for Au contacts) and a higher on-current of ≈50 μA μm^{-1} (compared with ≈30 μA μm^{-1} for Au

 © 2023 The Authors. Advanced Science published by Wiley-VCH GmbH

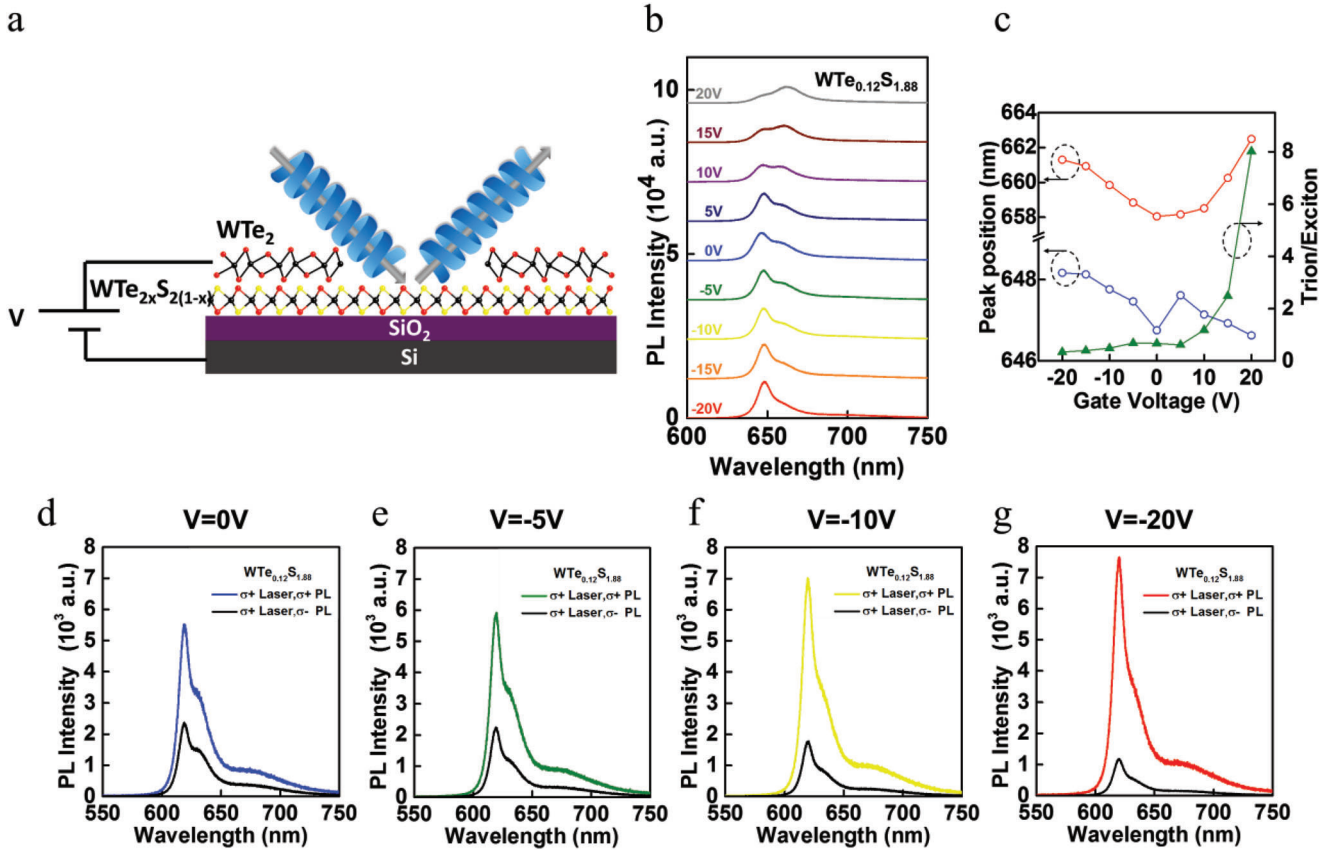

Figure 6. Electrically tunable valley polarization of $WTe_{0.12}S_{1.88}$ /1T′- WTe_2 with lowest SBH. a) Schematic illustration of a $WTe_2/WTe_{0.12}S_{1.88}$ heterostructure. b) PL spectra at RT for V_g values ranging from −20 V to 20 V, with an increment of 5 V. c) Gate voltage dependence of the PL peak position for neutral excitons (blue) and trions (red) under V_g from −20 V to 20 V. The intensity ratio of trions and excitons (green) is also shown as a function of V_g from −20 V to 20 V. The σ^+ (blue) and σ^- (black) PL intensity were taken at RT under d) $V_g = 0$, The σ^+ (green) and σ^- (black) PL intensity were taken at RT under e) $V_g = -5$ V. The σ^+ (yellow) and σ^- (black) PL intensity taken at RT under f) $V_g = -10$ V. The σ^+ (red) and σ^- (black) PL intensity taken at RT under g) $V_g = -20$ V.

contacts). These findings implied that the types of electrical contacts could substantially modify the FET characteristics.

To quantitatively investigate the SBH, the FET output characteristics were measured at different temperatures (200–300 K) and presented in Figure S8. The SBH ϕ_B can be extracted from the data by using the following thermionic emission model:[59–62]

$$\ln\left(\frac{I_0}{T^{3/2}}\right) = \ln(AA^*) - \frac{e\phi_B}{k_B T} \quad (6)$$

where A is the junction area, A^* is the effective Richardson-Boltzmann constant given by$A^* = 4\pi e m_n k_B^2/h^3$, m_n is the electronic effective mass of $WTe_{2x}S_{2(1-x)}$, and the effective "emission current" I_0 is obtained from the I_{ds}-versus-V_{ds} curves measured at different temperatures and gate voltages. Thus, we obtained ϕ_B at the two contacts/ $WTe_{2x}S_{2(1-x)}$ ($x < 0.5$) interfaces from the slop of the linear fit to ln $(I_0/T^{3/2})$ as a function of $1/(k_B T)$ (Figure 5c,d and Figure S7, Supporting Information). In Figure 5e, the effective SBH were extracted under the flat band gate voltage (V_g) condition, which corresponded to the start of deviation of the ϕ_B versus V_g curve from the linear slope. Figure 5f summarizes the relation between the SBH (at the V_{FB}) of the metal-semiconductor junction (MSJ) and the work functions of the Au and WTe_2 in contact with monolayer $WTe_{2x}S_{2(1-x)}$ alloys. The SBH between the Au electrode and $WTe_{0.12}S_{1.88}$ alloy was ≈150 meV, which confirmed the existence of Fermi-level pinning compared to the ideal Schottky-Mott rule theoretically calculated SBH (≈620 meV). In contrast, in the case of WTe_2 electrodes, the value of the SBH (≈80 meV) between 1T′-WTe_2 and $WTe_{0.12}S_{1.88}$ alloy was much closer to the ideal Schottky-Mott rule theoretically calculated SBH (≈20 meV) for monolayer $WTe_{0.12}S_{1.88}$-based FETs with 1T′-WTe_2 contacts. This finding revealed that WTe_2 electrical contacts weakened the Fermi level pinning and thus improved the electron charge injection to the $WTe_{0.12}S_{1.88}$ alloy substantially. Additionally, the SBW for the 1T′-WTe_2 contact can be estimated by using the built-in potential $V_{bi} = (\phi_M - \phi_s)/e = 0.02$ and $N_D \approx (1.3 \times 10^{11})$ cm^{-2} for the $WTe_{0.12}S_{1.88}$ alloy, which yields a small SBW ≈2.2 nm for 1T′-WTe_2 on $WTe_{0.12}S_{1.88}$.

Figure 6a shows a schematic of a back-gated FET device based on monolayer $WTe_{0.12}S_{1.88}$ alloy with WTe_2 electrode. For a given gate voltage, there were two well-defined PL spectral components associated with the emission bands of the neutral excitons (X) and the negatively charged trions (X^-). We found that the emission near 650 nm (≈1.91 eV) from neutral excitons (X) was

 © 2023 The Authors. Advanced Science published by Wiley-VCH GmbH

dominant around the charge neutrality point at $V_g = 0$. The PL spectral evolution of these two emission bands with gate voltage is illustrated in Figure 6b,c for the 1T′-WTe_2/1H-$WTe_{0.12}S_{1.88}$ device. We note that the trion-to-exciton intensity ratios of monolayer 1H-$WTe_{0.12}S_{1.88}$ exhibited dependence on the gate voltage, as shown in Figure 6c. The gate voltage-dependent DVP became significantly different in the case of 1H-$WTe_{0.12}S_{1.88}$ device with 1T′-WTe_2 electrodes. Figure 6b,c shows the PL spectral evolution of X and X^- emissions with gate voltage from the 1H-$WTe_{0.12}S_{1.88}$ device with WTe_2 electrodes. Additionally, polarization-resolved PL spectra of the 1H-$WTe_{0.12}S_{1.88}$ device with WTe_2 electrodes under σ^+excitations are shown in Figure 6d–g for $V_g = 0$, −5 V, −10 V and −20 V, respectively. For $V_g = 0$, which corresponded to the valley-polarized state in pristine 1H-$WTe_{0.12}S_{1.88}$ alloy, excitons at the K valley were more populated under σ^+ excitations with the DVP ≈40% as expected. By increasing the electron density via decreasing the gate voltage from 0 to −5 V, −10 V and −20 V, the difference between the σ^+ and σ^- components of the PL spectra became increasingly more significant, implying enhanced valley polarization of the neutral excitons. Specifically, we found that the values of DVP for $V_g = 0$, −5 V, −10 V, and −20 V were ≈40%, 45%, 50%, and 70%, respectively, suggesting significantly enhanced valley polarization as the applied bias moved away from the charge neutral point. Neutral excitons are the natural low-energy excitations of a charge-neutral semiconductor, whereas trions are only formed in the presence of excess charge. Therefore, the intensity of trion emissions is generally dependent on the amount of excess charge in the semiconductor. For this reason, trion emissions were usually not found in the PL spectra of our CVD-grown monolayer WS_2 samples unless a back gate voltage was applied. For the gated samples, the PL spectra typically exhibited additional emissions at 30–60 meV below the neutral excitonic line, which may be attributed to the emission from negatively charged trions (X^-). Thus, by simply varying the applied back gate voltage, we were able to control the ratio between neutral exciton and charged trion emissions.

To gain further insights into this behavior, we performed gate-dependent transport measurements, using a scheme where a positive bias induced hole-doping and a negative bias introduced electron-doping. We observed typical *n*-type transport behavior with on/off current ratios greater than 10^6 at room temperature, as shown in Figure S9. The doped carrier density $n = [(\epsilon\epsilon_0/t_{ox})(V_g - V_{CNP})/e]$ under gate voltage V_g was estimated, where $\epsilon = 3.9$ is the dielectric constant of SiO_2, t_{ox} is the thickness of SiO_2, and ϵ_0 is the vacuum permittivity. As shown in Figure S9, the charge neutral point (CNP) was observed to be at 20 V so that the *n*-type carrier concentration could be estimated, which yielded 1.5×10^{12} cm^{-2}, 1.89×10^{12} cm^{-2}, 2.27×10^{12} cm^{-2}, and 3.03×10^{12} cm^{-2} for 0 V, −5 V, −10 V, and −20 V, respectively. These values confirmed the notion that the enhancement of valley polarization by electrostatic doping in the $WTe_{0.12}S_{1.88}$ alloy may be attributed to carrier doping-induced suppression on the inter-valley relaxation process, because the inter-valley relaxation process of bright excitons is dominated by the long-range electron-hole (e-h) exchange interaction, and the long-range e-h exchange interactions may be efficiently screened by increasing the 2D carriers in the monolayer TMD with electrostatic doping. Here the screen length is determined by the inverse of the Thomas-Fermi wave vector[63] $k_{TF}(T, E_F) = k_{TF0}[1 - \exp(-\frac{E_F}{k_B T})]$, where $k_{TF0} = g_s g_v m^* e^2/(4\pi\epsilon\hbar^2)$ is the zero temperature Thomas-Fermi wave vector, g_s (g_v) is the degeneracy for spins (valleys), m^* is the effective electron or hole mass, and ϵ is the dielectric constant. The Fermi energy E_F measured from the bottom of the conduction band (to the top of the valance band) is defined by $E_F = 2\pi n\hbar^2/(g_s g_v m^*)$, where n is the doped 2D electron (hole) density. Therefore, k_{TF} increases rapidly with increasing n. In the strong scattering limit, the inter-valley scattering rate $(\tau_v)^{-1}$ due to e-h exchange interaction may be approximated by the relation $(\tau_v)^{-1} \propto (k_{TF})^{-2}$. Therefore, the inter-valley scattering rate $(\tau_v)^{-1}$is strongly suppressed by increasing carrier doping.[63] In contrast, the intra-valley relaxation time τ_0 is much less affected by carrier doping, as supported by the stable linewidths and integrated intensities upon doping. Noting that the valley polarization P_{DVP}[64,65] is given by

$$P_{DVP} = \frac{P_0}{1 + 2\left(\tau_0/\tau_v\right)} \tag{7}$$

with P_0 being the ideal valley polarization, we find that the suppression of $(\tau_v)^{-1}$by electrostatic doping leads to enhanced P_{DVP}, which agrees well with our experimental observations.

3. Conclusion

In this work, we presented new strategies to efficiently tailor the valley-polarized PL from semiconducting monolayer 1H-$WTe_{2x}S_{2(1-x)}$ at RT through chemical and electrostatic doping. We synthesized different compositions of monolayer $WTe_{2x}S_{2(1-x)}$ alloys ($0 \le x \le 1$) by alloying Te into tungsten disulfide WS_2 with a single-step APCVD method, and demonstrated a structural phase transition from the 1H semiconducting phase for $x < 0.5$ to the 1T′ metallic phase for $x > 0.5$. The compositions of the $WTe_{2x}S_{2(1-x)}$ alloys were identified by using XPS and Raman spectroscopic studies. The PL spectra revealed that the optical bandgap of the $WTe_{2x}S_{2(1-x)}$ alloy could be tuned from 2 to 1.75 eV in the 1H-semiconducting phase and then drop to 0 in the 1T′-metallic phase for $x > 0.5$. Additionally, studies of the FET devices based on monolayer $WTe_{2x}S_{2(1-x)}$ alloys confirmed that the 1H-phase alloys were *n*-type semiconductors and the 1T′-phase alloys were metals. We observed drastic enhancement of the DVP at RT from ~ 5% in WS_2 to ~ 40% in $WTe_{0.12}S_{1.88}$ alloy, and found that the DVP values in 1H-$WTe_{2x}S_{2(1-x)}$ correlated with the 2D carrier densities in the alloys. These findings may be attributed to (*i*) enhanced spin-orbit coupling due to Te-doping, and (*ii*) enhanced screening of the electron-hole exchanging interactions by increasing the carrier densities that resulted in reduced inter-valley scattering of excitons. By further applying a back-gate bias voltage (V_g) to monolayer 1H-$WTe_{0.12}S_{1.88}$-based FETs with 1T′-WTe_2 electrodes that exhibited the lowest Schottky barrier height, we were able to further enhance the DVP value from ≈40% for $V_g = 0$ to ≈70% for $V_g = -20$ V, which corroborated with the notion that excess carriers provided efficient screening of the momentum-dependent long-range electron-hole exchange interaction and led to reduced intervalley scattering. The methodology described in this work thus provides a promising platform to tailor the valley degree of freedom in 1H-TMD alloys efficiently at RT, paving ways for investigating various fundamental physical

 © 2023 The Authors. Advanced Science published by Wiley-VCH GmbH

properties in 2D-TMD materials (e.g., new types of TMD-based Wyle semimetals, spin Hall effects, opto-valleytronic and opto-spintronic characteristics) and for future applications of valley-dependent optoelectronic devices in energy-efficient information processing.

4. Experimental Section

Synthesis of $WTe_{2x}S_{2(1-x)}$: $WTe_{2x}S_{2(1-x)}$ was grown by atmosphere-pressure chemical vapor deposition (APCVD). Sulfur (S) and tellurium (Te) powders were placed into two quartz boats. The amount of sulfur was fixed at 10 mg, while the amount of Te was adjusted according to the weight ratio from 1 to 10. 95 mg of WO_3 precursor mixed with 5 mg of KI was placed in a quartz boat containing the SiO_2/Si substrates set face-down directly above the W source precursor, and the quartz boat was then positioned upstream at 8 cm away from the Te source. A sulfur boat was placed upstream at 18 cm away from the center of the furnace and a tellurium boat was placed downstream at 5 cm away from the S source. Next, the system was pumped down to 3×10^{-2} torr to eliminate air and moisture. After the system reached the base pressure, the Ar/H_2 (80/40 sccm) carrier gas was introduced until atmospheric pressure was achieved. The furnace was then heated up with a ramp rate of 35 °C min^{-1} to the growth temperatures (750 to 850 °C). The S component melted at 150 °C and the Te component melted at 450 °C were sent into the furnace at the growth temperature to grow $WTe_{2x}S_{2(1-x)}$. The sample growth procedure proceeded for 10 minutes, after which the furnace was directly opened to room temperature to stop the reaction immediately.

Synthesis of WS_2: Monolayer WS_2 was grown using APCVD as previously reported. 95 mg of WO_3 precursor mixed with 5 mg of KI was placed in a quartz boat containing the SiO_2/Si substrates set face-down directly above the W source precursor, and the quartz boat was then positioned at the center of the furnace. A second boat containing 100 mg S was placed upstream at 18 cm away from the W source. Next, the system was pumped down to 3×10^{-2} torr to eliminate air and moisture. After the system reached the base pressure, the Ar/H_2 (80/40 sccm) carrier gas was introduced until atmospheric pressure was achieved. The furnace was then heated up with a ramp rate of 35 °C min^{-1} to the growth temperatures (750 to 850 °C). The S component melted at 150 °C was sent into the furnace at the growth temperature to grow WS_2. The sample growth procedure proceeded for 10 minutes, after which the furnace was directly opened to room temperature to stop the reaction immediately.

Synthesis of WTe_2: Multilayer WTe_2 was grown using APCVD. 120 mg of WO_3 precursor mixed with 15 mg of KI was placed in a quartz boat containing the SiO_2/Si substrates set face-down directly above the W source precursor, and the quartz boat was then positioned at the center of the furnace. A second boat containing 500 mg Te was placed upstream at 10 cm away from the W source. Next, the system was pumped down to 3×10^{-2} torr to eliminate air and moisture. After the system reached the base pressure, the Ar/H_2 (80/40 sccm) carrier gas was introduced until atmospheric pressure was achieved. The furnace was then heated up with a ramp rate of 35 °C min^{-1} to the growth temperatures (775 to 800 °C). The Te component melted at 450 °C was sent into the furnace at the growth temperature to grow WTe_2. The sample growth procedure proceeded for 25 minutes, after which the furnace was directly opened to room temperature to stop the reaction immediately.

Metal Transfer Process: A 4-inch SiO_2/Si wafer with a 300 nm-thick oxide layer was first functionalized with an OH group by the following squence: The SiO_2/Si wafers were dipped into 80°C piranha solution (H_2SO_4 : H_2O_2 = 3:1) for 2 h to render the surface of the substrates hydrophilic, which were subsequently washed with deionized water and dried with nitrogen gas. Next, the SiO_2/Si wafers were cleaned with O_2 plasma (300 mTorr, 10 sccm, and 100 W) for 10 min. Finally, the wafers were soaked in 60°C H_2O_2 solution for 60 min to become superhydrophilic on the surface. The functionalized surface of SiO_2/Si, as schematically shown in Figure S5, Supporting Information, was used for the growth of $WTe_{2x}S_{2(1-x)}$ alloys and for the deposition of metal electrodes. The gold deposited on the functionalized surface of SiO_2/Si was patterned into electrodes by conventional e-beam lithography (Figure S5c, Supporting Information). The patterned gold electrodes on the SiO_2/Si wafer was then spin-coated with a polystyrene (PS) or poly(methhyl methacrylate) (PMMA) layer (Figure S5d) followed by slow immersion into deionized (DI) water for the transfer (Figure S5e). Water instantly penetrated through the PS/Au or PMMA/Au stack. The growth substrate with a higher surface energy compared to the polymer/Au stack led to easy delamination and suspension of the polymer/Au stack on the surface of water. Thus, polymer-supported wafer-scale Au electrodes were achieved in the form of a stack, which was subsequently transferred onto the $WTe_{2x}S_{2(1-x)}$ alloy (Figure S5e–g, Supporting Information) for the fabrication of FETs.

XPS and UPS Measurements: XPS and UPS studies were performed under ultra-high vacuum (residual gas pressure 5×10^{-9} torr) with a Kratos AXIS Ultra DLD and a magnetic immersion lens that consisted of a spherical mirror and concentric hemispherical analyzers with a delay-line detector (DLD). An Al Kα (1.486 KeV) monochromatic source and He 1 (21.2 eV) source were used as excitation sources for the XPS and UPS measurements, respectively. Ejected electrons were collected at a 90° angle from the horizontal.

Raman and PL Characterizations: The Raman and PL spectra were taken with a Renishaw InVia Raman spectrometer system using a 514.3 nm laser (2.41 eV) as the excitation source. A 50× objective lens with a numerical aperture of 0.75 and a 2400 lines mm^{-1} and 1800 lines mm^{-1} grating were chosen during the measurement to achieve a better signal-to-noise ratio.

STEM Characterization: The cross-sectional sample for the TEM experiments was prepared using a dual beam-focused ion beam (FIB)/SEM system (SMI3050SE, SEIKO). HR-TEM and SAED were performed using a field emission transmission electron microscope (JEM-2100F, Joel) with an acceleration voltage of 100 kV.

Device Fabrication and Measurements: $WTe_{2x}S_{2(1-x)}$ field-effect transistors (FETs) were fabricated using standard electron-beam (E-beam) lithography techniques. First, the $WTe_{2x}S_{2(1-x)}$ monolayer flakes were transferred on a heavily p-doped Si substrate with 300 nm thick SiO_2 layer, which served as a bottom gate and a gate dielectric, respectively. The metallic contact electrodes were fabricated by E-beam lithography, and 200 nm Au contact electrodes were deposited on silanol functionalized SiO_2/Si substrate using E-beam evaporation. The channel length (L) and width (W) of the fabricated devices were 0.5 µm and 1 µm. The metallic contact electrodes were transferred and aligned on top of the $WTe_{2x}S_{2(1-x)}$ monolayer flake using our metal transferred method described earlier under the paragraph of metal transfer process. To transfer WTe_2 contacts onto the $WTe_{2x}S_{2(1-x)}$ monolayer flakes, the synthesized WTe_2 films were first transferred onto the silanol functionalized SiO_2/Si substrates by the PMMA-assisted wet-transferred method. Next, the WTe_2 electrodes were patterned using E-beam lithography and oxygen plasma treatment (10 sccm O_2 gas, 20 mtorr, and 80 W) that selectively etched away the exposed WTe_2 regions. The WTe_2 patterns (L = 0.5 µm and L = 1 µm) were subsequently transferred onto the $WTe_{2x}S_{2(1-x)}$ monolayer flake on a Si/SiO_2 substrate using the transferred method. The electrical properties of $WTe_{2x}S_{2(1-x)}$ FETs were studied using a Keithley 2636 sourcemeter as a DC voltage source in vacuum at 200 –300 K.

Acknowledgements

This work was jointly supported by the Army Research Office under the Multi-University Research Initiative (MURI) program (award #W911NF-16-1-0472) and the National Science Foundation under the Physics Frontier Center program for Institute for Quantum Information and Matter (IQIM) at the California Institute of Technology (award #1733907). The authors also acknowledged support from the Beckman Institute at the California Institute of Technology for access to facilities at the Molecular Materials Research Center. W.-H. Lin thanks Ruohan Wang for great discussion and support and acknowledged a graduate fellowship from the J. Yang Family Foundation. C.-S. Li acknowledges the support from the

 © 2023 The Authors. Advanced Science published by Wiley-VCH GmbH

Ministry of Science and Technology in Taiwan (award #108-2911-I-002-524 and 109-2622-8-002-003) for his visit and research at Caltech.

Conflict of Interest

The authors declare no conflict of interest.

Author Contributions

W.-H.L. and N.-C.Y. conceived the research ideas. W.-H.L. and C.-S.L. contributed equally to this work. W.-H.L. constructed the CVD system for WS_2, WTe_2, and $WTe_{2x}S_{2(1-x)}$ growth and participated in all the measurements and data analysis. W.-H.L. and H.A.A. contributed to the XPS measurement. W.-H.L., C.-S.L., and G.R.R. contributed to the Raman and PL mapping measurements. W.-H.L., C.-S.L., and C.I.W. contributed to the FET device measurements. W.-H.L. and N.-C.Y. wrote the manuscript, and N.-C.Y. supervised and coordinated the project.

Data Availability Statement

The data that support the findings of this study are available from the corresponding author upon reasonable request.

Keywords

circular dichroism, field-effect transistors, phase transition, ternary tellurides, transition metal dichalcogenides, tunable bandgaps, valleytronics, $WTe_{2x}S_{2(1-x)}$

Received: July 18, 2023
Revised: September 25, 2023
Published online: November 16, 2023

[1] K. F. Mak, C. Lee, J. Hone, J. Shan, T. F. Heinz, *Phys. Rev. Lett.* **2010**, *105*, 136805.
[2] A. Splendiani, L. Sun, Y. Zhang, T. Li, J. Kim, C.-Y. Chim, G. Galli, F. Wang, *Nano Lett.* **2010**, *10*, 1271.
[3] S. Z. Butler, S. M. Hollen, L. Cao, Y. Cui, J. A. Gupta, H. R. Gutiérrez, T. F. Heinz, S. S. Hong, J. Huang, A. F. Ismach, E. Johnston-Halperin, M. Kuno, V. V. Plashnitsa, R. D. Robinson, R. S. Ruoff, S. Salahuddin, J. Shan, L. Shi, M. G. Spencer, M. Terrones, W. Windl, J. E. Goldberger, *ACS Nano* **2013**, *7*, 2898.
[4] R. Ganatra, Q. Zhang, *ACS Nano* **2014**, *8*, 4074.
[5] J. K. Huang, J. Pu, C. L. Hsu, M. H. Chiu, Z.-Y. Juang, Y.-H. Chang, W. H. Chang, Y. Iwasa, T. Takenobu, L. J. Li, *ACS Nano* **2014**, *8*, 923.
[6] F. Xia, H. Wang, D. Xiao, M. Dubey, A. Ramasubramaniam, *Nat. Photonics* **2014**, *8*, 899.
[7] Q. H. Wang, K. Kalantar-Zadeh, A. Kis, J. N. Coleman, M. S. Strano, *Nat. Nanotechnol.* **2012**, *7*, 699.
[8] H. Zeng, J. Dai, W. Yao, D. Xiao, X. Cui, *Nat. Nanotechnol.* **2012**, *7*, 490.
[9] K. F. Mak, K. He, J. Shan, T. F. Heinz, *Nat. Nanotechnol.* **2012**, *7*, 494.
[10] T. Cao, G. Wang, W. Han, H. Ye, C. Zhu, J. Shi, Q. Niu, P. Tan, E. Wang, B. Liu, J. Feng, *Nat. Commun.* **2012**, *3*, 887.
[11] D. Xiao, G. B. Liu, W. Feng, X. Xu, W. Yao, *Phys. Rev. Lett.* **2012**, *108*, 196802.
[12] G. Wang, A. Chernikov, M. M. Glazov, T. F. Heinz, X. Marie, T. Amand, B. Urbaszek, *Rev. Mod. Phys.* **2018**, *90*, 021001.
[13] W. H. Lin, W. S. Tseng, C. M. Went, M. L. Teague, G. R. Rossman, H. A. Atwater, N. C. Yeh, *ACS Nano* **2020**, *14*, 1350.
[14] D. Xiao, W. Yao, Q. Niu, *Phys. Rev. Lett.* **2007**, *99*, 236809.
[15] W. Yao, D. Xiao, Q. Niu, *Phys. Rev. B* **2008**, *77*, 235406.
[16] J. S. Ross, S. Wu, H. Yu, N. J. Ghimire, A. M. Jones, G. Aivazian, J. Yan, D. G. Mandrus, D. Xiao, W. Yao, X. Xu, *Nat. Commun.* **2013**, *4*, 1474.
[17] W. H. Lin, P. C. Wu, H. Akbari, G. R. Rossman, N. C. Yeh, H. A. Atwater, *Adv. Mater.* **2022**, *34*, 2104863.
[18] W. Zheng, P. Fan, D. Zhang, B. Zheng, C. Ge, Y. Chen, B. Xu, Z. Tang, J. Liu, T. Zhang, Y. Jiang, X. Wang, X. Zhu, S. Chen, Q. Yuan, A. Pan, *Sci. China Mater.* **2022**, *65*, 2502.
[19] S. Liu, A. Granados Del Águila, X. Liu, Y. Zhu, Y. Han, A. Chaturvedi, P. Gong, H. Yu, H. Zhang, W. Yao, Q. Xiong, *ACS Nano* **2020**, *14*, 9873.
[20] J. Dang, M. Yang, X. Xie, Z. Yang, D. Dai, Z. Zuo, C. Wang, K. Jin, X. Xu, *Small* **2022**, *18*, 2106029.
[21] G. Liu, X. Zheng, H. Liu, J. Yin, C. Ke, W. Yang, Y. Wu, Z. Wu, X. Li, C. Zhang, J. Kang, *ACS Appl. Mater. Interfaces* **2021**, *13*, 35097.
[22] L. Du, M. Liao, G. B. Liu, Q. Wang, R. Yang, D. Shi, Y. Yao, G. Zhang, *Phys. Rev. B* **2019**, *99*, 195415.
[23] S. Das, H. Y. Chen, A. V. Penumatcha, J. Appenzeller, *Nano Lett.* **2013**, *13*, 100.
[24] H. Yuan, G. Cheng, L. You, H. Li, H. Zhu, W. Li, J. J. Kopanski, Y. S. Obeng, A. R. Hight Walker, D. J. Gundlach, C. A. Richter, D. E. Ioannou, Q. Li, *ACS Appl. Mater. Interfaces* **2015**, *7*, 1180.
[25] W. Park, Y. Kim, U. Jung, J. H. Yang, C. Cho, Y. J. Kim, S. M. N. Hasan, H. G. Kim, H. B. R. Lee, B. H. Lee, *Adv. Electron. Mater.* **2016**, *2*, 1500278.
[26] Y. Kim, W. Park, J. H. Yang, C. Cho, S. K. Lee, B. H. Lee, *Phys. Status Solidi (RRL) – Rapid Res. Lett.* **2016**, *10*, 634.
[27] H. Fang, M. Tosun, G. Seol, T. C. Chang, K. Takei, J. Guo, A. Javey, *Nano Lett.* **2013**, *13*, 1991.
[28] Y. Du, H. Liu, A. T. Neal, M. Si, P. D. Ye, *IEEE Electron Device Lett.* **2013**, *34*, 1328.
[29] L. Yang, K. Majumdar, H. Liu, Y. Du, H. Wu, M. Hatzistergos, P. Y. Hung, R. Tieckelmann, W. Tsai, C. Hobbs, P. D. Ye, *Nano Lett.* **2014**, *14*, 6275.
[30] M. H. D. Guimarães, H. Gao, Y. Han, K. Kang, S. Xie, C. J. Kim, D. A. Muller, D. C. Ralph, J. Park, *ACS Nano* **2016**, *10*, 6392.
[31] M. W. Iqbal, M. Z. Iqbal, M. F. Khan, M. A. Kamran, A. Majid, T. Alharbi, J. Eom, *RSC Adv.* **2016**, *6*, 24675.
[32] H. M. W. Khalil, M. F. Khan, J. Eom, H. Noh, *ACS Appl. Mater. Interfaces* **2015**, *7*, 23589.
[33] J. Xu, J. Shim, J.-H. Park, S. Lee, *Adv. Funct. Mater.* **2016**, *26*, 5328.
[34] Q. Ji, C. Li, J. Wang, J. Niu, Y. Gong, Z. Zhang, Q. Fang, Y. Zhang, J. Shi, L. Liao, X. Wu, L. Gu, Z. Liu, Y. Zhang, *Nano Lett.* **2017**, *17*, 4908.
[35] W. S. Leong, Q. Ji, N. Mao, Y. Han, H. Wang, A. J. Goodman, A. Vignon, C. Su, Y. Guo, P.-C. Shen, Z. Gao, D. A. Muller, W. A. Tisdale, J. Kong, *J. Am. Chem. Soc.* **2018**, *140*, 12354.
[36] H. G. Shin, H. S. Yoon, J. S. Kim, M. Kim, J. Y. Lim, S. Yu, J. H. Park, Y. Yi, T. Kim, S. C. Jun, S. Im, *Nano Lett.* **2018**, *18*, 1937.
[37] S. S. Chee, D. Seo, H. Kim, H. Jang, S. Lee, S. P. Moon, K. H. Lee, S. W. Kim, H. Choi, M.-H. Ham, *Adv. Mater.* **2019**, *31*, 1804422.
[38] Y. Liu, P. Stradins, S.-H. Wei, *Sci. Adv.* **2016**, *2*, e1600069.
[39] W. G. Dawson, D. W. Bullett, *J. Phys. C: Solid State Phys.* **1987**, *20*, 6159.
[40] S. Song, S.-Y. Kim, J. Kwak, Y. Jo, J. H. Kim, J. H. Lee, J. U. Lee, J. U. Kim, H. D. Yun, Y. Sim, J. Wang, D. H. Lee, S. H. Seok, T.-I. Kim, H. Cheong, Z. Lee, S. Y. Kwon, *Adv. Sci.* **2019**, *6*, 1801370.
[41] M. J. Mleczko, A. C. Yu, C. M. Smyth, V. Chen, Y. C. Shin, S. Chatterjee, Y.-C. Tsai, Y. Nishi, R. M. Wallace, E. Pop, *Nano Lett.* **2019**, *19*, 6352.
[42] S. J. Yun, G. H. Han, H. Kim, D. L. Duong, B. G. Shin, J. Zhao, Q. A. Vu, J. Lee, S. M. Lee, Y. H. Lee, *Nat. Commun.* **2017**, *8*, 2163.

 © 2023 The Authors. Advanced Science published by Wiley-VCH GmbH

[43] J. Zhou, F. Liu, J. Lin, X. Huang, J. Xia, B. Zhang, Q. Zeng, H. Wang, C. Zhu, L. Niu, X. Wang, W. Fu, P. Yu, T. R. Chang, C. H. Hsu, D. Wu, H. T. Jeng, Y. Huang, H. Lin, Z. Shen, C. Yang, L. Lu, K. Suenaga, W. Zhou, S. T. Pantelides, G. Liu, Z. Liu, *Adv. Mater.* **2017**, *29*, 1603471.
[44] A. M. Jones, H. Yu, N. J. Ghimire, S. Wu, G. Aivazian, J. S. Ross, B. Zhao, J. Yan, D. G. Mandrus, D. Xiao, W. Yao, X. Xu, *Nat. Nanotech.* **2013**, *8*, 634.
[45] J. R. Schaibley, H. Yu, G. Clark, P. Rivera, J. S. Ross, K. L. Seyler, W. Yao, X. Xu, *Nat. Rev. Mater.* **2016**, *1*, 16055.
[46] G. Wang, C. Robert, A. Suslu, B. Chen, S. Yang, S. Alamdari, I. C. Gerber, T. Amand, X. Marie, S. Tongay, B. Urbaszek, *Nat. Commun.* **2015**, *6*, 10110.
[47] K. M. Mccreary, A. T. Hanbicki, G. G. Jernigan, J. C. Culbertson, B. T. Jonker, *Sci. Rep.* **2016**, *6*, 19159.
[48] Y. C. Jiang, J. Gao, L. Wang, *Sci. Rep.* **2016**, *6*, 19624.
[49] S. J. R. Tan, I. Abdelwahab, Z. Ding, X. Zhao, T. Yang, G. Z. J. Loke, H. Lin, I. Verzhbitskiy, S. M. Poh, H. Xu, C. T. Nai, W. Zhou, G. Eda, B. Jia, K. P. Loh, *J. Am. Chem. Soc.* **2017**, *139*, 2504.
[50] L. Liu, J. Wu, L. Wu, M. Ye, X. Liu, Q. Wang, S. Hou, P. Lu, L. Sun, J. Zheng, L. Xing, L. Gu, X. Jiang, L. Xie, L. Jiao, *Nat. Mater.* **2018**, *17*, 1108.
[51] A. Berkdemir, H. R. Gutiérrez, A. R. Botello-Méndez, N. Perea-López, A. L. Elías, C. I. Chia, B. Wang, V. H. Crespi, F. López-Urías, J. C. Charlier, H. Terrones, M. Terrones, *Sci. Rep.* **2013**, *3*, 1755.
[52] A. P. S. Gaur, S. Sahoo, J. F. Scott, R. S. Katiyar, *J. Phys. Chem. C* **2015**, *119*, 5146.
[53] Y. C. Lin, C. H. Yeh, H.-C. Lin, M. D. Siao, Z. Liu, H. Nakajima, T. Okazaki, M. Y. Chou, K. Suenaga, P.-W. Chiu, *ACS Nano* **2018**, *12*, 12080.
[54] J. Kang, S. Tongay, J. Li, J. Wu, *J. Appl. Phys.* **2013**, *113*, 143703.
[55] X. Duan, C. Wang, A. Pan, R. Yu, X. Duan, *Chem. Soc. Rev.* **2015**, *44*, 8859.
[56] Y. Ding, Y. Wang, J. Ni, L. Shi, S. Shi, W. Tang, *Phys. B* **2011**, *406*, 2254.
[57] Y. Yue, J. Chen, Y. Zhang, S. Ding, F. Zhao, Y. Wang, D. Zhang, R. Li, H. Dong, W. Hu, Y. Feng, W. Feng, *ACS Appl. Mater. Interfaces* **2018**, *10*, 22435.
[58] Z. Q. Xu, Y. Zhang, S. Lin, C. Zheng, Y. L. Zhong, X. Xia, Z. Li, P. J. Sophia, M. S. Fuhrer, Y.-B. Cheng, Q. Bao, *ACS Nano* **2015**, *9*, 6178.
[59] A. R. Jang, *Nanomaterials* **2022**, *12*, 3038.
[60] S. W. Lagasse, P. Dhakras, K. Watanabe, T. Taniguchi, J. U. Lee, *Adv. Mater.* **2019**, *31*, 1901392.
[61] C. Kim, I. Moon, D. Lee, M. S. Choi, F. Ahmed, S. Nam, Y. Cho, H. J. Shin, S. Park, W. J. Yoo, *ACS Nano* **2017**, *11*, 1588.
[62] B. K. Kim, T. H. Kim, D. H. Choi, H. Kim, K. Watanabe, T. Taniguchi, H. Rho, J.-J. Kim, Y. H. Kim, M.-H. Bae, *npj 2D Mater. Appl.* **2021**, *5*, 9.
[63] S. Konabe, *Appl. Phys. Lett.* **2016**, *109*, 073104.
[64] S. Mouri, Y. Miyauchi, K. Matsuda, *Nano Lett.* **2013**, *13*, 5944.
[65] S. Feng, C. Cong, S. Konabe, J. Zhang, J. Shang, Y. Chen, C. Zou, B. Cao, L. Wu, N. Peimyoo, B. Zhang, T. Yu, *Small* **2019**, *15*, 1805503.

 © 2023 The Authors. Advanced Science published by Wiley-VCH GmbH